

## Spacecraft Observations of Oblique Electron Beams Breaking the Frozen-In Law During Asymmetric Reconnection

J. Egedal,<sup>1</sup> A. Le,<sup>2</sup> W. Daughton,<sup>2</sup> B. Wetherton,<sup>1</sup> P. A. Cassak,<sup>3</sup> J. L. Burch,<sup>4</sup> B. Lavraud,<sup>5</sup>  
J. Dorelli,<sup>6</sup> D. J. Gershman,<sup>6</sup> and L. A. Avanov<sup>6</sup>

<sup>1</sup>*Department of Physics, University of Wisconsin-Madison, Madison, Wisconsin 53706, USA*

<sup>2</sup>*Los Alamos National Laboratory, Los Alamos, New Mexico 87545, USA*

<sup>3</sup>*Department of Physics and Astronomy, West Virginia University, Morgantown, West Virginia 26506, USA*

<sup>4</sup>*Southwest Research Institute, San Antonio, Texas 78238, USA*

<sup>5</sup>*Institut de Recherche en Astrophysique et Planétologie, Université de Toulouse, UMR 5277, Toulouse, France*

<sup>6</sup>*Heliophysics Science Division, NASA Goddard Space Flight Center, Greenbelt, Maryland 20771, USA*



(Received 5 December 2017; published 29 January 2018)

Fully kinetic simulations of asymmetric magnetic reconnection reveal the presence of magnetic-field-aligned beams of electrons flowing toward the topological magnetic  $x$  line. Within the  $\sim 6d_e$  electron-diffusion region, the beams become oblique to the local magnetic field, providing a unique signature of the electron-diffusion region where the electron frozen-in law is broken. The numerical predictions are confirmed by *in situ* Magnetospheric Multiscale spacecraft observations during asymmetric reconnection at Earth's dayside magnetopause.

DOI: 10.1103/PhysRevLett.120.055101

Magnetic reconnection is the process that changes the magnetic field line topology in plasma [1]. Within the framework of ideal magneto-hydro-dynamics (MHD), which describes the large-scale and long-time dynamics of a perfectly conducting plasma, magnetic reconnection is forbidden, as it requires a violation of the ideal MHD frozen-in law. The frozen-in law states that the plasma and magnetic field always move together, which often provides a remarkably accurate description of the macroscopic dynamics of space plasma. The topological constraint on the magnetic field is also a consequence of this frozen-in law, which causes magnetic stress and narrow current layers to build in a variety of plasma systems. The stored energy can then be released explosively when reconnection is triggered in small diffusion regions, often involving kinetic plasma effects at microscopic scales [2].

Well-known examples of explosive reconnection include both solar flare events [3] and reconnection in Earth's magnetotail [4], where it is the driver of the aurora borealis [1]. Meanwhile, reconnection at Earth's dayside magnetopause is less sporadic and has recently been investigated by NASA's Magnetospheric Multiscale (MMS) mission [5] specially designed to characterize the plasma dynamics within the fine spatial scales of the reconnection region [6–8]. The separation between the four MMS spacecraft ( $\approx 10$  km) is smaller than the expected size of the ion-diffusion region (on the order of  $d_i = c/\omega_{pi} \approx 40$  km), but much larger than  $d_e \approx 1$  km characteristic of the electron-diffusion region, and it remains challenging to assess whether a spacecraft has made an electron-diffusion region crossing. For example, while crescent-shaped

electron distributions [6,9,10] indicate proximity of a reconnection site, these distributions are linked to density gradients reaching beyond the electron-diffusion region [11].

In this Letter, we study field-aligned electron beams that stream towards the  $x$  line within the ion-diffusion region in a 2D fully kinetic simulation. As a unique signature of electron demagnetization and the breakdown of the frozen-in law, these beams become oblique to the magnetic field as the field lines turn sharply within the electron-diffusion region. We demonstrate how these unique signatures were captured by the MMS4 spacecraft during the reconnection event reported by Burch *et al.* [6].

The kinetic simulation is performed with the VPIC code [12] using asymptotic parameters approximating those of Ref. [6]. The simulation is periodic in  $L$  and has conducting boundaries in  $N$ , with a total size of  $4032 \times 4032$  cells =  $20d_i \times 20d_i$ , initialized with approximately 400 particles per cell. Here  $N$  and  $L$  are defined in Fig. 1. More details on the run are available in Ref. [11]. Within the ion diffusion region the electron dynamics are closely related to the structure of the magnetic field. In asymmetric reconnection the typical quadrupolar Hall perturbation of the out-of-plane magnetic field is suppressed along the low-density separatrices [13,14]. With Figs. 1(a) and 1(b) we observe that a field ratio  $B_M/B_N \approx 0.5$  is typical for the inner reconnection region. Consequently, as is also evident from the selected 3D magnetic field lines, the magnetic field lines approximately lie in the  $xz$  plane illustrated in Fig. 1(b), spanned by the unit vectors  $\mathbf{e}_x = (\mathbf{e}_N + 0.5\mathbf{e}_M)/\sqrt{1 + 0.5^2}$  and  $\mathbf{e}_z = \mathbf{e}_L$ .

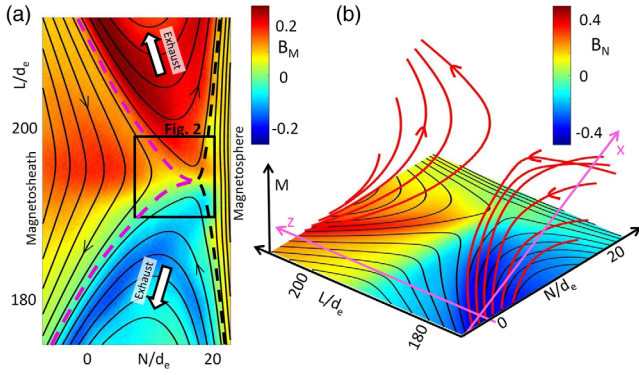


FIG. 1. (a) Simulation profile of the out-of-plane  $B_M$  magnetic field. The high (low) density separatrices are indicated by the magenta (black) dashed lines. (b) Profile of the normal magnetic field  $B_N$ . As shown by the selected field lines, because  $B_M/B_N \approx 0.5$  in much of the region, the magnetic field approximately lies in the  $xz$  plane defined in the figure.

We use cuts of the electron distribution function,  $f_e$ , in the  $xz$  plane for analyzing the electron behavior near the topological  $x$  line. For the  $10d_e \times 10d_e$  region outlined by the black square in Fig. 1(a), the panels in Fig. 2 present

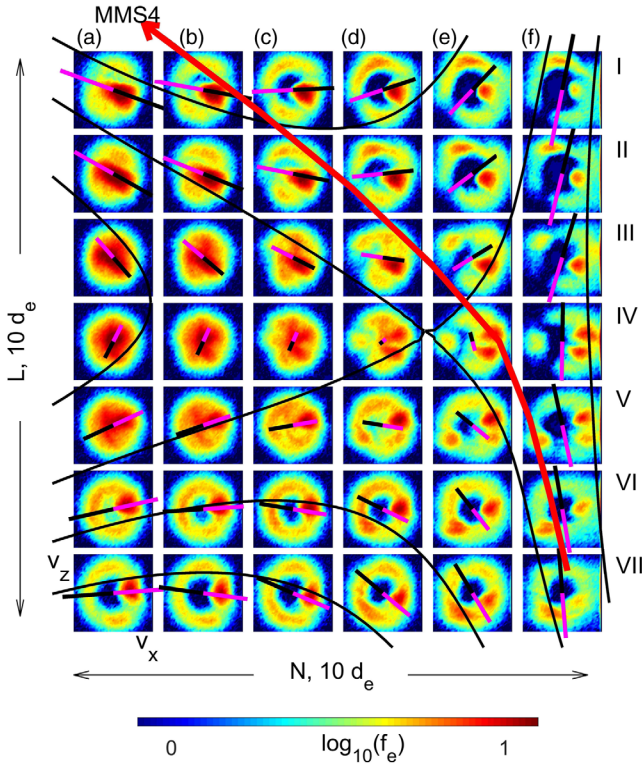


FIG. 2. Cuts of electron distributions in the  $xz$  plane ( $v_y = 0$ ) defined in Fig. 1(b). The distributions are obtained on the  $10d_e \times 10d_e$  region marked in Fig. 1(a). The magnetic field lies mostly in the  $xz$  plane and its components are indicated by the magenta or black lines in the panels. As a signature of the electron-diffusion region, the parallel beams streaming in along the magnetic field in columns (a)–(c) do not follow the direction of the magnetic field as the field rotates sharply in columns (d)–(f).

$v_x - v_z$  cuts of  $f_e(\mathbf{v})$ . The indicated trajectory of MMS4 will be discussed below.

The distribution in Fig. 2(a), panel II, elongated in the directions parallel and antiparallel to the magnetic field, is typical for inflows in symmetric reconnection, mainly composed of trapped electrons energized by magnetic-field-aligned (parallel) electric fields [15–17]. However, because of the strong curvature of the magnetic field lines in the high-density inflow, the magnetic field radius of curvature can become smaller than the typical electron Larmor radius, such that the magnetic moment is not well conserved as an adiabatic invariant [18]. As is particularly evident in panels III–IV of Figs. 2(a) and 2(b), the associated pitch angle mixing causes the distributions in some regions of the high-density inflow to become nearly isotropic [19].

Because of the electrons’ low mass, their thermal motion along magnetic field lines is rapid, and the electrons close to the  $x$  line are mainly sourced by the field-aligned beams observed along the high-density separatrix (such as panel II of Figs. 2(a) and 2(b)) streaming into the  $x$ -line region. The incoming beams are also observed in the two exhaust regions [i.e., panels I and VII of Fig. 2(b)], but the beams are here superposed with ring-shaped features of slightly energized electrons. These “ring” electrons have already interacted with the electron-diffusion region and are now mostly streaming away from the region along the magnetic field lines. In symmetric reconnection similar distributions are observed along all four arms of the separatrix [20,21], where the beams also are generated by direct  $E_{\parallel}$  energization [22] of incoming electrons.

A key result pertains to the behavior of the field-aligned beams as they reach the  $x$ -line region. The incoming beams within the exhausts for Figs. 2(a)–2(c) are nearly perfectly aligned with the magnetic field. However, in Figs. 2(d)–2(f) the field rotates so sharply that the beams do not follow the direction of the field; rather, due to their inertia the beams continue to flow in the directions set in Figs. 2(a)–2(c). Thus, the inertia of the parallel streaming carries the electrons across the in-plane magnetic field as it turns sharply from being mainly in the  $x$  direction to approximately the  $z$  direction. Similar to guide-field reconnection [23], as a special feature for the distribution in panel IV of Figs. 2(e) and 2(f), we observe two distinct incoming beams. Confirmed by orbit tracking, these originate from the two separate arms of the high-density separatrix.

A prominent and compelling feature of the “Burch event” [6] is the observation of two flavors (parallel and perpendicular) of crescent-shaped electron distribution functions. The perpendicular crescent shapes are observed in simulations [24,25] and predicted based on 1D reasoning [9,10]. More generally, both perpendicular and parallel crescent distributions can be expected in regions of strong density gradients present along the separatrix between the magnetospheric low-density inflow and the exhaust regions

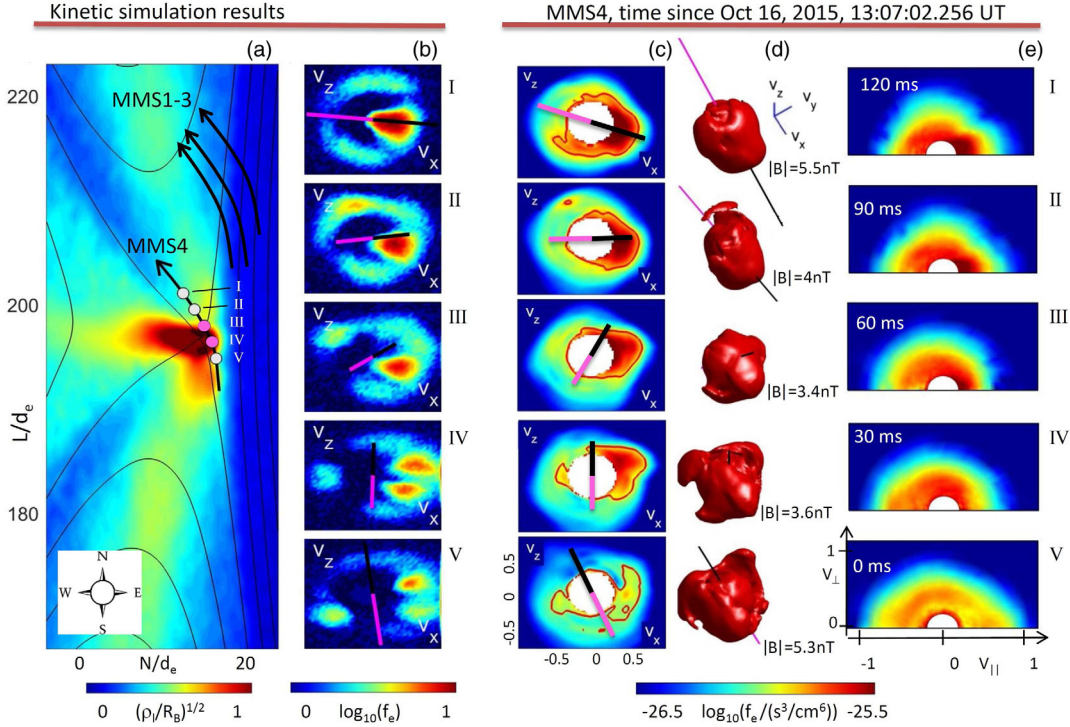


FIG. 3. (a) Color contours of constant  $\sqrt{\rho_{le}/R_B}$ , where for  $\sqrt{\rho_{le}/R_B} > 0.5$  the electron magnetic moment breaks down as an adiabatic invariant. Approximate paths of MMS1-4 for the October 16, 2015 event are indicated. For the five selected points along the MMS4 path, cuts of the electron distribution are shown in (b) in the format of Fig. 2. (c)–(e) Electron distributions measured by MMS4 shown in three different representations, with the velocity axes normalized by  $v_0 = 10^7$  m/s. The cuts in (c) provide a close match to the numerical distributions in (b).

[11], and are not a conclusive signature of the electron diffusion region [26,27].

Through an analysis of the magnetic fields recorded during the Burch event, Denton *et al.* [28] showed that MMS4 traveled the closest to the  $x$  line. Here we use the electron distributions measured by MMS4 to further constrain the trajectory of MMS4 through the simulation shown in Fig. 2 and Fig. 3(a). It is noted how the five points marked along the trajectory in Fig. 3(a) provide a qualitative match to those in Figs. 3(c)–3(e) observed by MMS4. For reasons given below, we consider the two points highlighted in magenta to be within the electron-diffusion region.

The color contours in Fig. 3(a) show the magnitude of  $\sqrt{\rho_{le}/R_B}$  in the simulation, where  $\rho_{le}$  is the typical electron Larmor radius and  $R_B$  is the radius of curvature of the magnetic field. For  $\sqrt{\rho_{le}/R_B} > 0.5$  the electron magnetic moment breaks down as an adiabatic invariant, and the electrons are effectively demagnetized [18]. The format of the distributions in Fig. 3(b) is identical to that used in Fig. 2. For the point deepest into the exhaust in Fig. 3(b), panel I, we observe an incoming beam well aligned with the magnetic field direction. In panels II–IV of Fig. 3(b) the direction of the magnetic field turns by approximately  $90^\circ$ , while the beam directions are observed to be virtually unchanged. As discussed above, for the point just to the right of the  $x$  line, the distribution in Fig. 3(b), panel IV,

includes two mixed beams originating from the two arms of the high-density separatrix. The distribution in Fig. 3(b), panel V, is for a point sufficiently inside the low-density inflow that the beam electrons become remagnetized, and in field-aligned coordinates (not shown here), this distribution displays crescent-shaped characteristics [11].

The distributions in Figs. 3(c)–3(e) were recorded by MMS4 over a time interval of 120 ms. The distribution in panel V of Figs. 3(c)–3(e) was the last parallel crescent-shaped distribution observed by MMS4 at  $t = 13:07:02.256$ , denoted  $t = 0$  in Fig. 3(e). The parallel crescent shape is clearly visible in the  $f(v_{\parallel}, v_{\perp})$  representation of Fig. 3(e), panel V. Unique for MMS4, the crescent shaped distributions are observed with  $v_z < 0$  corresponding to electron streaming southward away from the  $x$  line [6]. This suggests (contrary to the conclusion of Ref. [29]) that MMS4 at  $t = 0$  was located close to the magnetospheric separatrix to the southeast of the topological  $x$  line.

Similar to the numerical distributions in Fig. 3(b), the MMS4 distributions in Fig. 3(c) are  $v_x v_z$  cuts where the  $x$  direction is determined by the magnetic field direction recorded at  $t = 30$  ms and the  $z$  direction is determined by requiring the magnetic field to lie in the  $xz$  plane for  $t = 90$  ms. As is the case for the simulation distributions, during the full sequence the magnetic field mostly lies in the  $xz$  plane. The direction and strength of the measured

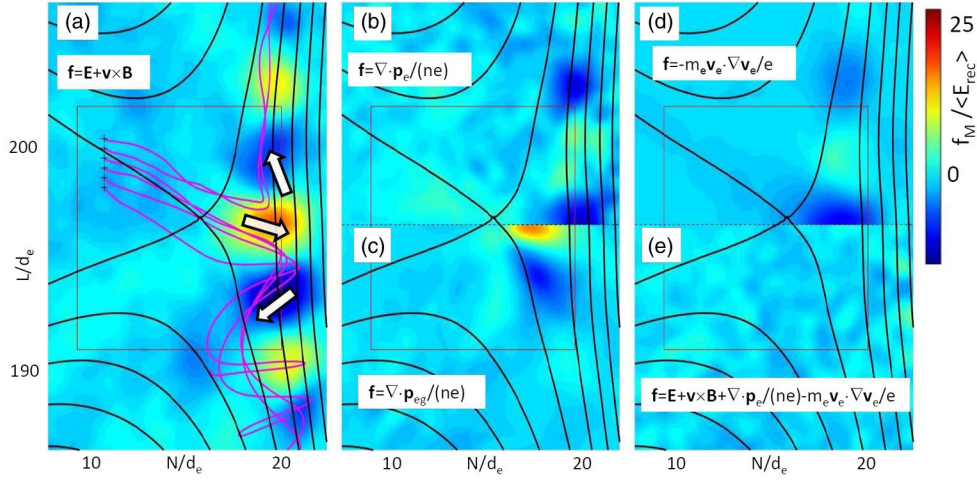


FIG. 4. Color contours of constant  $f_M / \langle E_{\text{rec}} \rangle$ , where  $\mathbf{f}$  represents terms or sums of terms in the electron momentum balance equations, as indicated in the panels. The trajectories in (a) are initialized with  $\mathbf{v} = 1.5v_{th}\mathbf{b}$  and illustrate the behavior for the center of the incoming beam distributions. The three white arrows show the general direction of the electron beams near the  $x$  line, and are consistent with  $\mathbf{v}_N \times \mathbf{B}_L$  driving the modulations observed in  $f_M = (\mathbf{E} + \mathbf{v} \times \mathbf{B})_M$ .

$\mathbf{B}_{xz}$  field are indicated by the magenta or black lines in Fig. 3(c), and they closely match the magnetic field behavior in Fig. 3(b) for the inferred trajectory through the simulation profiles.

The measured distribution in Fig. 3(c), panel I, displays a clear field-aligned beam similar to that in the simulation, and places MMS4 to the northwest of the  $x$  line. Furthermore, as is the case in the simulation, the beam is observed to persist in panels II–IV of Fig. 3(c) with nearly unchanged direction while the magnetic field rotates by approximately  $90^\circ$ . Figure 3(d) show 3D isosurfaces of the MMS distributions corresponding to the phase-space value indicated by the red contour levels in Fig. 3(c). Again, similar to the simulation results, the distribution in panel IV of Figs. 3(c) and 3(d) for  $t = 30$  contains features consistent with mixing of two incoming beams, providing further evidence that MMS4 is here observing the actual electron-diffusion region.

While other studies suggest that 3D effects are important for heating in the magnetospheric inflow [30–32], the agreement between our numerical results and the details of the MMS4 observations suggests that fundamental properties of the electron-diffusion region are well represented by 2D kinetic simulations. The speed of MMS4 relative to the  $x$  line is 100 km/s, predominantly in the  $L$  direction [28]. Thus, also consistent with the expectations from the numerical simulation, the  $\approx 60$  ms encounter with the electron-diffusion region of panels III–IV of Figs. 3(c)–3(e) corresponds to an approximate diffusion region size of about  $6 \text{ km} \approx 6d_e$ .

An outstanding question in reconnection is centered on the out-of-plane force balance of the electron fluid near the  $x$  line, seeking a theoretical understanding of how the forces associated with the  $E_M$  electric field ( $= E_{\text{rec}}$  at the  $x$  line) can be accounted for by effects not included in ideal MHD. During quasisteady reconnection, partial time derivative

terms become negligible such that the momentum balance is governed by a generalized Ohm’s law of the form

$$\mathbf{E} + \mathbf{v}_e \times \mathbf{B} + \frac{1}{ne} \nabla \cdot \mathbf{p}_e - \frac{m_e}{e} \mathbf{v}_e \cdot \nabla \mathbf{v}_e = 0, \quad (1)$$

where  $\mathbf{p}_e = m_e \int (\mathbf{u} - \mathbf{v}_e)(\mathbf{u} - \mathbf{v}_e) f_e(\mathbf{u}) d^3u$  is the electron pressure tensor.

In Fig. 4 we examine the role of the incoming beams on the reconnection region momentum balance. To distinguish between gyrotropic and nongyrotropic contributions we introduce the gyrotropic pressure tensor  $\mathbf{p}_{eg} = \mathbf{b}\mathbf{b}p_{e\parallel} + (\mathbf{I} - \mathbf{b}\mathbf{b})p_{e\perp}$ , with  $p_{e\parallel} = \mathbf{b} \cdot \mathbf{p}_e \cdot \mathbf{b}$  and  $p_{e\perp} = [\text{trace}(\mathbf{p}_e) - p_{e\parallel}]/2$ . The color contours in Fig. 4(a) correspond to the out-of-plane component  $f_M / \langle E_{\text{rec}} \rangle$ , with  $\mathbf{f} = \mathbf{E} + \mathbf{v}_e \times \mathbf{B}$ . Periodic modulations of  $f_M$  are observed particularly strongly on the low-density side of the separatrix. The amplitude of the modulation exceeds  $10\langle E_{\text{rec}} \rangle$ , where  $\langle E_{\text{rec}} \rangle$  is the time average of the reconnection electric field for the period where reconnection is observed in the simulation.

To investigate the origin of these modulation, we consider the magenta trajectories in Fig. 4(a), typical for incoming electrons. The trajectories are initialized with  $\mathbf{v} = v_{\text{beam}}\mathbf{b}$ , where  $v_{\text{beam}} = 1.5v_{th}$  is characteristic for the beams in Fig. 2. The modulations in  $f_M$  are in phase with the  $v_N$  of these trajectories, yielding the strong  $\mathbf{v}_e \times \mathbf{B}$  force in the  $M$  direction. The amplitude of the  $f_M$  modulations decline quickly as phase mixing destroys the coherency of the trajectories at values of  $L$  further away from the  $x$  line. In Ref. [33] similar structures were observed and interpreted as standing nonlinear whistler waves.

Figures 4(b)–(d) shows color contours representing the magnitude of various terms in the electron momentum equation. The nongyrotropic stress in  $\mathbf{p}_e$  includes significant contributions to the electron-momentum-balance equation

near the electron-diffusion region where the electron dynamics is not well characterized by guiding center theory [11]. The magnitudes of the full pressure term,  $\nabla \cdot \mathbf{p}_e/ne$ , and inertia term,  $m_e \mathbf{v}_e \cdot \nabla \mathbf{v}_e/e$  are similar, but the latter dominates the important region within  $1d_e$  of the topological  $x$  line. Finally, in Fig. 4(e) we illustrate how the sum of all terms is approximately zero, consistent with electron momentum balance being described by Eq. (1). Again, given the correlation between the modulations in  $f_M$  and the typical beam trajectories, we conclude that the incoming beams are responsible for the large amplitudes of the terms  $\mathbf{v}_e \times \mathbf{B}$ ,  $\nabla \cdot \mathbf{p}_e/ne$ , and  $m_e \mathbf{v}_e \cdot \nabla \mathbf{v}_e/e$ .

In summary, for the considered 2D kinetic simulation of asymmetric reconnection, the distributions in the inner electron-diffusion region include strong electron beams. These beams are generated by direct  $E_{\parallel}$  acceleration along the arms of the high-density separatrix and are directed along the local magnetic field in toward the  $x$  line. Because of the inertia of the beams, they do not follow the direction of the magnetic field as it rotates sharply within the electron-diffusion region. The diffusion region of antiparallel asymmetric reconnection is therefore characterized by electron beams at oblique directions to the local magnetic field. The trajectories of the beams through the diffusion region are correlated with strong perturbations of nonideal terms in the electron force balance equations, breaking the frozen-in condition.

The described numerical results provide a qualitative match to detailed observations of MMS4 recorded during the Burch event of October 16, 2015 [6]. In a time span of 60 ms (corresponding to  $\sim 6$  km) the electron distributions recorded by MMS4 transition from parallel crescent distributions, to distributions with oblique electron beams, and then to distributions with field aligned incoming electron beams. The experimentally observed sequence of electron distributions as well as magnetic field strength and rotation is accurately matched by assuming a trajectory through the simulation's electron-diffusion region. This agreement is direct evidence that MMS4 encountered the electron-diffusion region, and suggests that 2D kinetic simulations include the dominant reconnection dynamics, sufficient to account for salient details of the  $\sim 6d_e$  electron-diffusion region of a naturally occurring 3D system.

J. E. acknowledges the support by the National Science Foundation (NSF) GEM Award No. 1405166, A. L. acknowledges NASA Grant No. NNX14AL38G, and simulations used NASA HEC and LANL IC resources.

[1] J. Dungey, *Philos. Mag.* **44**, 725 (1953).

[2] E. G. Zweibel and M. Yamada, *Annu. Rev. Astron. Astrophys.* **47**, 291 (2009).

- [3] S. Krucker, H. S. Hudson, L. Glesener, S. M. White, S. Masuda, J. P. Wuelser, and R. P. Lin, *Astrophys. J.* **714**, 1108 (2010).
- [4] M. Øieroset, T. Phan, M. Fujimoto, R. P. Lin, and R. P. Lepping, *Nature (London)* **412**, 414 (2001).
- [5] J. L. Burch, T. E. Moore, R. B. Torbert, and B. L. Giles, *Space Sci. Rev.* **199**, 5 (2016).
- [6] J. L. Burch *et al.*, *Science* **352**, aaf2939 (2016).
- [7] L. J. Chen *et al.*, *J. Geophys. Res.* **122**, 5235 (2017).
- [8] S. A. Fuselier *et al.*, *J. Geophys. Res.* **122**, 5466 (2017).
- [9] M. A. Shay, T. D. Phan, C. C. Haggerty, M. Fujimoto, J. F. Drake, K. Malakit, P. A. Cassak, and M. Swisdak, *Geophys. Res. Lett.* **43**, 4145 (2016).
- [10] N. Bessho, L.-J. Chen, and M. Hesse, *Geophys. Res. Lett.* **43**, 1828 (2016).
- [11] J. Egedal *et al.*, *Phys. Rev. Lett.* **117**, 185101 (2016).
- [12] K. Bowers, B. Albright, L. Yin, W. Daughton, V. Roytershteyn, B. Bergen, and T. Kwan, *J. Phys. Conf. Ser.* **180**, 012055 (2009).
- [13] H. Karimabadi, D. Krauss-Varban, N. Omid, and H. Vu, *J. Geophys. Res.* **104**, 12313 (1999).
- [14] K. G. Tanaka *et al.*, *Ann. Geophys.* **26**, 2471 (2008).
- [15] J. Egedal, M. Øieroset, W. Fox, and R. P. Lin, *Phys. Rev. Lett.* **94**, 025006 (2005).
- [16] J. Egedal, W. Fox, N. Katz, M. Porkolab, M. Øieroset, R. P. Lin, W. Daughton, and J. F. Drake, *J. Geophys. Res.* **113**, A12207 (2008).
- [17] J. Egedal, A. Le, and W. Daughton, *Phys. Plasmas* **20**, 061201 (2013).
- [18] J. Buchner and L. Zelenyi, *J. Geophys. Res.* **94**, 11821 (1989).
- [19] B. Lavraud *et al.*, *Geophys. Res. Lett.* **43**, 3042 (2016).
- [20] T. Nagai, I. Shinohara, M. Fujimoto, M. Hoshino, Y. Saito, S. Machida, and T. Mukai, *J. Geophys. Res.* **106**, 25929 (2001).
- [21] Y. Asano *et al.*, *J. Geophys. Res.* **113**, A01207 (2008).
- [22] J. Egedal, W. Daughton, and A. Le, *Nat. Phys.* **8**, 321 (2012).
- [23] M. Hesse, L. J. Chen, Y. H. Liu, N. Bessho, and J. L. Burch, *Phys. Rev. Lett.* **118**, 145101 (2017).
- [24] M. Hesse, N. Aunai, D. Sibeck, and J. Birn, *Geophys. Res. Lett.* **41**, 8673 (2014).
- [25] L.-J. Chen, M. Hesse, S. Wang, N. Bessho, and W. Daughton, *Geophys. Res. Lett.* **43**, 2405 (2016).
- [26] H. Karimabadi, W. Daughton, and J. Scudder, *Geophys. Res. Lett.* **34**, L13104 (2007).
- [27] M. A. Shay, J. F. Drake, and M. Swisdak, *Phys. Rev. Lett.* **99**, 155002 (2007).
- [28] R. E. Denton, B. U. Ö. Sonnerup, H. Hasegawa, T. D. Phan, C. T. Russell, R. J. Strangeway, B. L. Giles, and R. B. Torbert, *J. Geophys. Res.* **121**, 9880 (2016).
- [29] H. Hasegawa *et al.*, *Geophys. Res. Lett.* **44**, 4566 (2017).
- [30] R. E. Ergun *et al.*, *Phys. Rev. Lett.* **116**, 235102 (2016).
- [31] L. Price, M. Swisdak, J. F. Drake, P. A. Cassak, J. T. Dahlin, and R. E. Ergun, *Geophys. Res. Lett.* **43**, 6020 (2016).
- [32] A. Le, W. Daughton, L. J. Chen, and J. Egedal, *Geophys. Res. Lett.* **44**, 2096 (2017).
- [33] M. Swisdak, J. Drake, L. Price, J. Burch, P. Cassak, and T. Phan, arXiv:1710.04555.